Supporting Information

Electronically modulated bimetallic telluride nano dendrites atop 2D nanosheets using a vanadium dopant enabling a bifunctional electrocatalyst for overall water splitting

Ishwor Pathak[a,b], Alagan Muthurasu[a], Debendra Acharya[a], Kisan Chhetri[a], Bipeen Dahal[c], Yagya Raj Rosyara[a], Taewoo Kim[a], Tae Hoon Ko[a]*, Hak Yong Kim [a,d] *

[a] Department of Nano Convergence Engineering, Jeonbuk National University, Jeonju, 54896, Republic of Korea

[b] Department of Chemistry, Amrit Campus, Tribhuvan University, Kathmandu 44613, Nepal

[c] Central Department of Chemistry, Tribhuvan University, Kathmandu 44613, Nepal

[d] Department of Organic Materials and Fiber Engineering, Jeonbuk National University, Jeonju 561-756, Republic of Korea

Corresponding Author's Email: khy@jbnu.ac.kr / taehoon222@naver.com

Materials

Cobalt nitrate hexahydrate ($Co(NO_3)_2.6H_2O$, 98.0%), sodium molybdate dihydrate ($Na_2MoO_4.2H_2O$, ≥99.0%), vanadium (III) chloride (VCl_3, 97.0%), ammonium fluoride (NH_4F, ≥98.0%), and tellurium powder (99.8%) were purchased from Sigma–Aldrich Co., St. Louis, MO, USA. Urea (NH_2CONH_2, ≥99.0%), ethanol (99.5%), and nitric acid (HNO_3, 60.0%) were obtained from Samchun Co. Ltd., Seoul, Korea. All chemicals were of analytical grade and were used without further purification. Deionized (DI) water purified through a Millipore-Q system was used to form aqueous solutions during the experiment.

Electrochemical characterization

Calculation of potential vs. RHE:

As we measure the potentials of the working electrodes in reference to the Ag/AgCl electrode, it is necessary to convert the working potential with respect to the reversible hydrogen electrode (RHE) using standard calibrations as described by the Nernst equation:

$$E_{RHE} = E_{Ag/AgCl} + 0.0596 \times pH + E^{\circ}_{Ag/AgCl} \quad (1)$$

where E_{RHE} = calculated potential vs. RHE, $E_{Ag/AgCl}$ = measured potential vs. Ag/AgCl, $E^{\circ}_{Ag/AgCl}$ = standard electrode potential of Ag/AgCl electrode (0.197 V at 25 °C), and pH = 13.5-14 for 1 M KOH.

iR correction:

The potential values obtained after LSV measurements were iR corrected using the following equation.

$$E_{iR\ corrected} = E_{(vs.\ RHE)} - i \times R_s \quad (2)$$

where i = current density R_s = resistance of the electrolytic solution (obtained from the EIS Nyquist plot).

Overpotential (η) calculation:

The overpotential of electrocatalysts at a particular current density can be calculated as follows:

$\eta_{OER} = E_{RHE} - 1.23$ V (3)

$\eta_{HER} = E_{RHE} - 0$ V (4)

Tafel slope:

The reaction kinetics of the electrocatalyst were analyzed from the following Tafel equation:

$\eta = a + b\log j$ (5)

where η, b, and j are the overpotential, Tafel slope, and current density, respectively. The Tafel slope represents the inherent quality of electrocatalysts, especially addressing the kinetics of the reaction.

Electrochemically active surface area (ECSA):

$$\text{ECSA} = C_{dl}/C_s \quad (6)$$

where, C_{dl} and C_s represent the electrical double layer capacitance and specific capacitance of the electrode surface, respectively. The ECSA is directly proportional to C_{dl}.

Calculation of Faradic efficiency (ηF):

The Faradaic efficiency **(ηF)** of the alkaline electrolyzer, utilizing V-$CoTe_2$/$MoTe_2$@CC as a bifunctional electrocatalyst was assessed by measuring the volumes of evolved H_2 and O_2 at the cathode and anode, respectively, in a lab-made H-cell. The H-cell electrolyzer was operated at a constant current density of 10 mA cm^{-2} for up to 120 minutes. The theoretical volumes of evolved H_2 and O_2 gases were estimated using Faraday's law:

$$V_{Theoritical} = \frac{IRTt}{PzF} \quad (7)$$

$V_{Theoritical} =$ Theoretical volume of gas evolution

$I =$ operating current density (mA cm^{-2})

$R =$ universal gas constant (0.0821 atm. L mol^{-1} K^{-1})

$t =$ operating time in seconds (s)

$T =$ temperature on the Kelvin scale (K)

$p =$ pressure (atm.)

$z =$ number of electrons involved in the production of 1 mole of O_2 ($z = 4$) or H_2 ($z = 2$)

$F =$ Faraday's constant ($F = 96{,}485\ C$)

ηF can be determined from the following equation: the ratio of the exact volume of real gas ($V_{Experimental}$) to the theoretical volume ($V_{Theoretical}$) during the reaction.

$$\eta F = \frac{V_{Experimental}}{V_{Theoretical}} * 100\% \quad (8)$$

where $V_{Experimental}$ is the volume of O_2 and H_2 gas evolved under a pressure of 1 atm at 300 K upon applying a current density of 10 mA cm^{-2}.

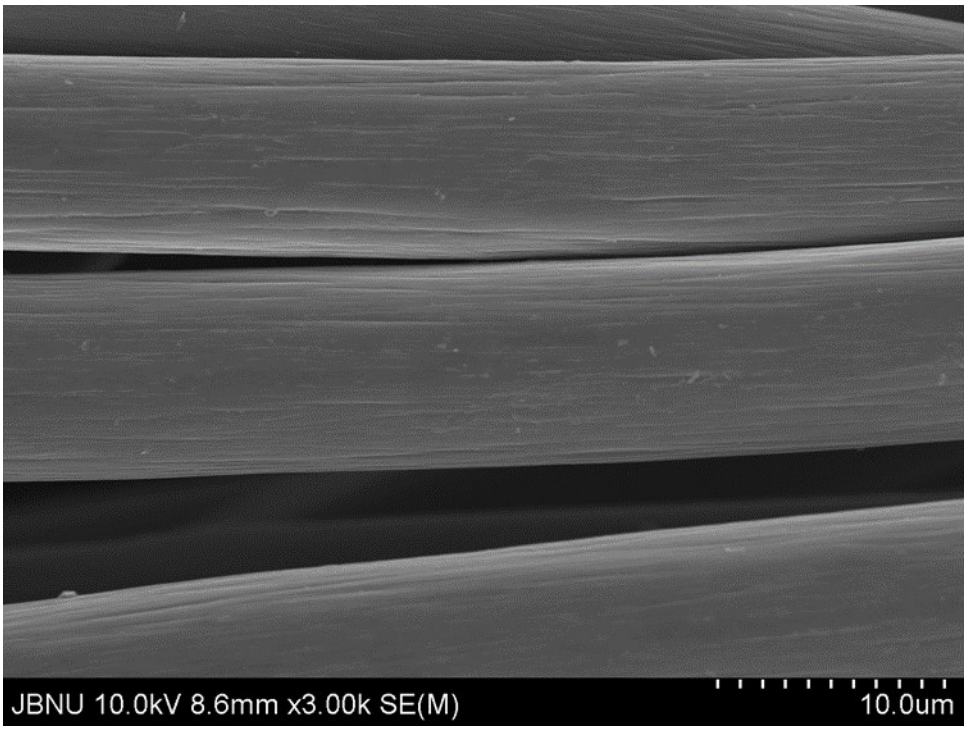

Fig. S1. FESEM image of bare carbon cloth (activated).

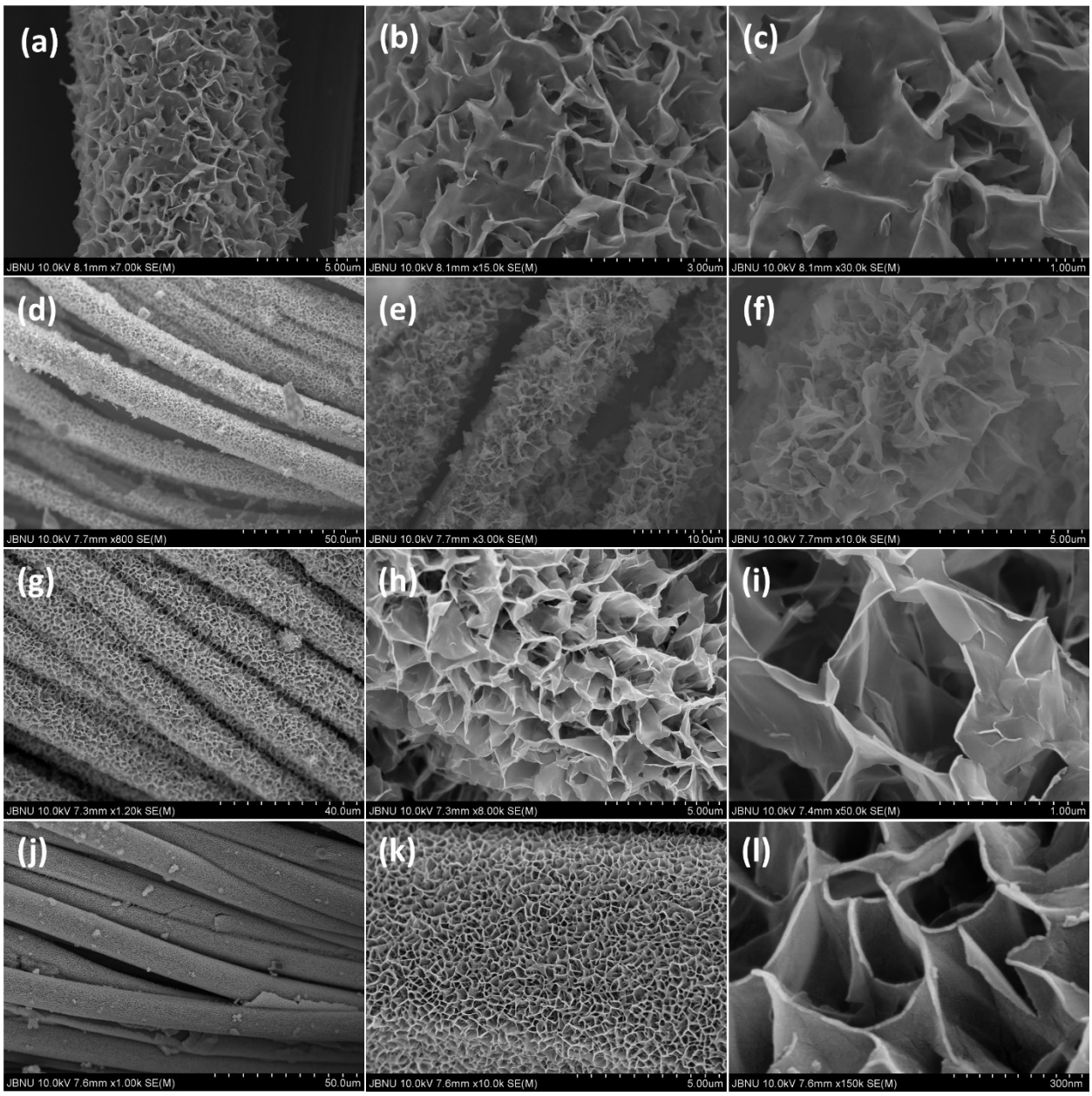

Fig. S2. FESEM image of V-CoMoOH@CC grown at different hydrothermal conditions. (a-c) 110 °C, 4 h, (d-f) 130 °C, 8 h (g-i) 130 °C, 5 h and (j-l) 120 °C, 6 h.

The hydrothermal conditions for the optimal growth of the V-CoMoOH nanosheets adhered to carbon clothes were determined by varying the heating temperature and holding time. V-CoMoOH nanosheets were not properly grown when heated to 110 °C for 4 h (**Fig. S2a-c**), possibly due to insufficient time and temperature for self-assembly. The V-CoMoOH nanosheets are not homogenous and the uniformity was destroyed upon heating at a relatively higher temperature (130 °C) for 8h (**Fig. 2d-f**). The V-CoMoOH was grown homogenously at 130 °C, 5

h, however, the nanosheet size was not uniform throughout the material (**Fig. 2g-i)**. Homogenously grown uniform nanosheets are clearly observed upon maintaining the hydrothermal condition of 120 °C for 6 h (**Fig. 2j-l)**, which is considered an optimized condition.

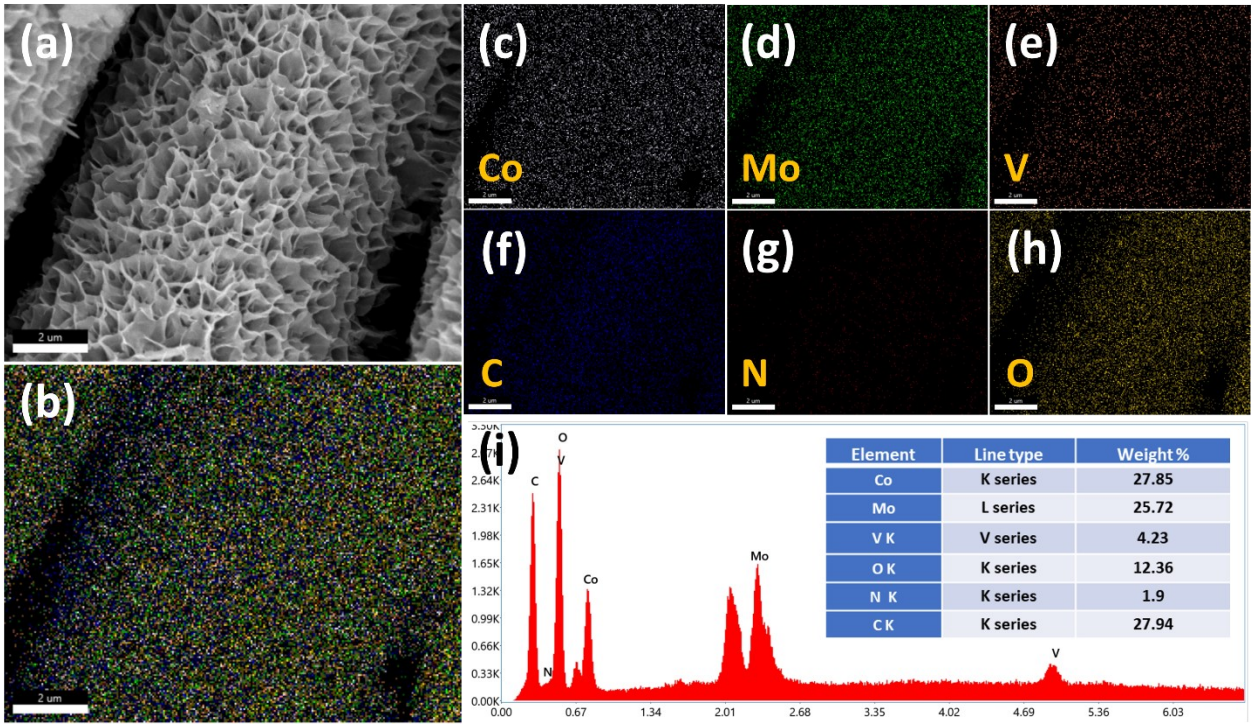

Element	Line type	Weight %
Co	K series	27.85
Mo	L series	25.72
V K	V series	4.23
O K	K series	12.36
N K	K series	1.9
C K	K series	27.94

Fig. S3. EDX analysis of V-CoMoOH@CC. (a) Elemental mapping area, (b) superimposition of all elements, and elemental mapping spectra of (c) Co, (d) Mo, (e) V, (f) C (g) N, and (h) O, and (i) EDX spectrum (inset: element %).

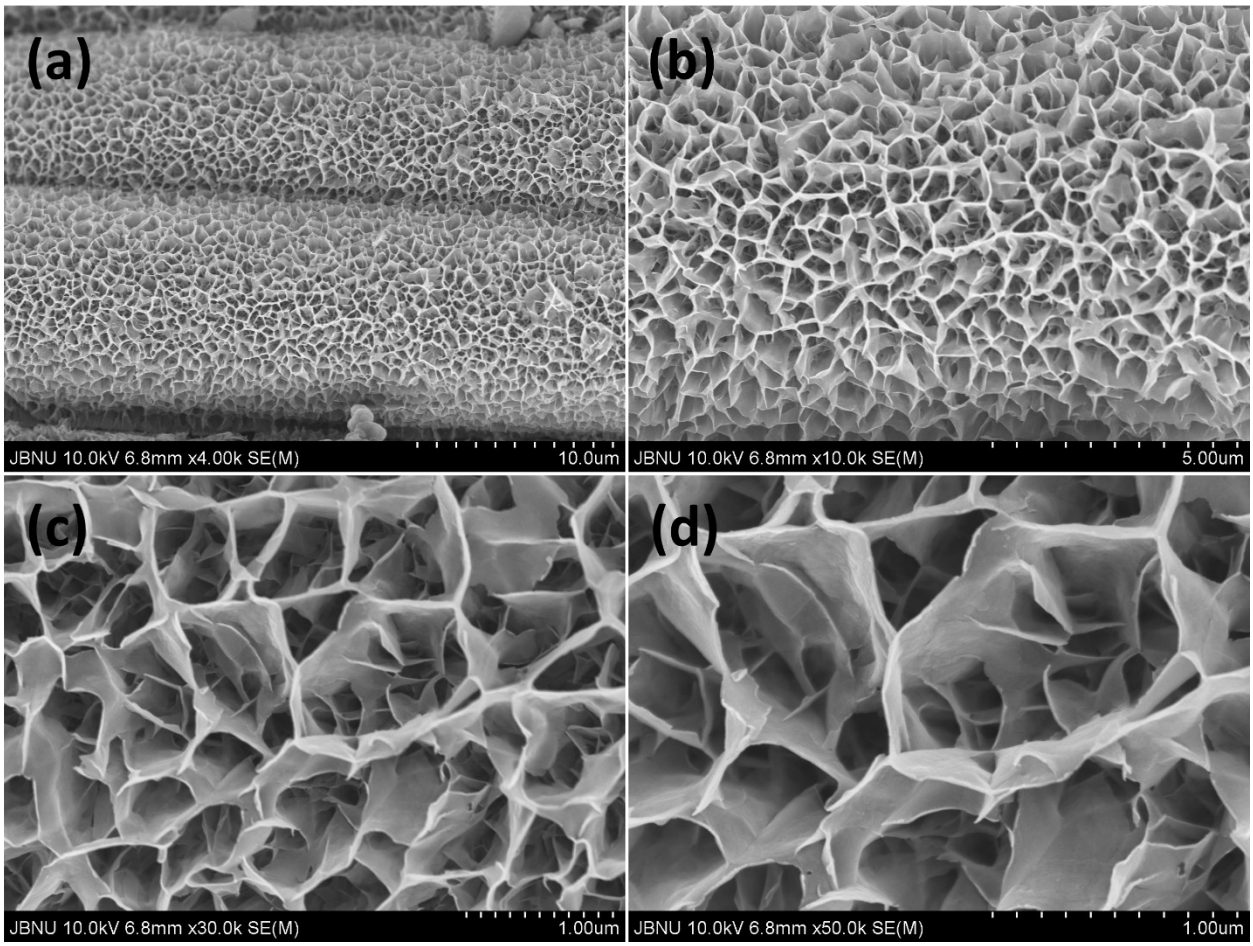

Fig. S4. (a-d) FESEM image of CoMoOH@CC at increasing magnifications.

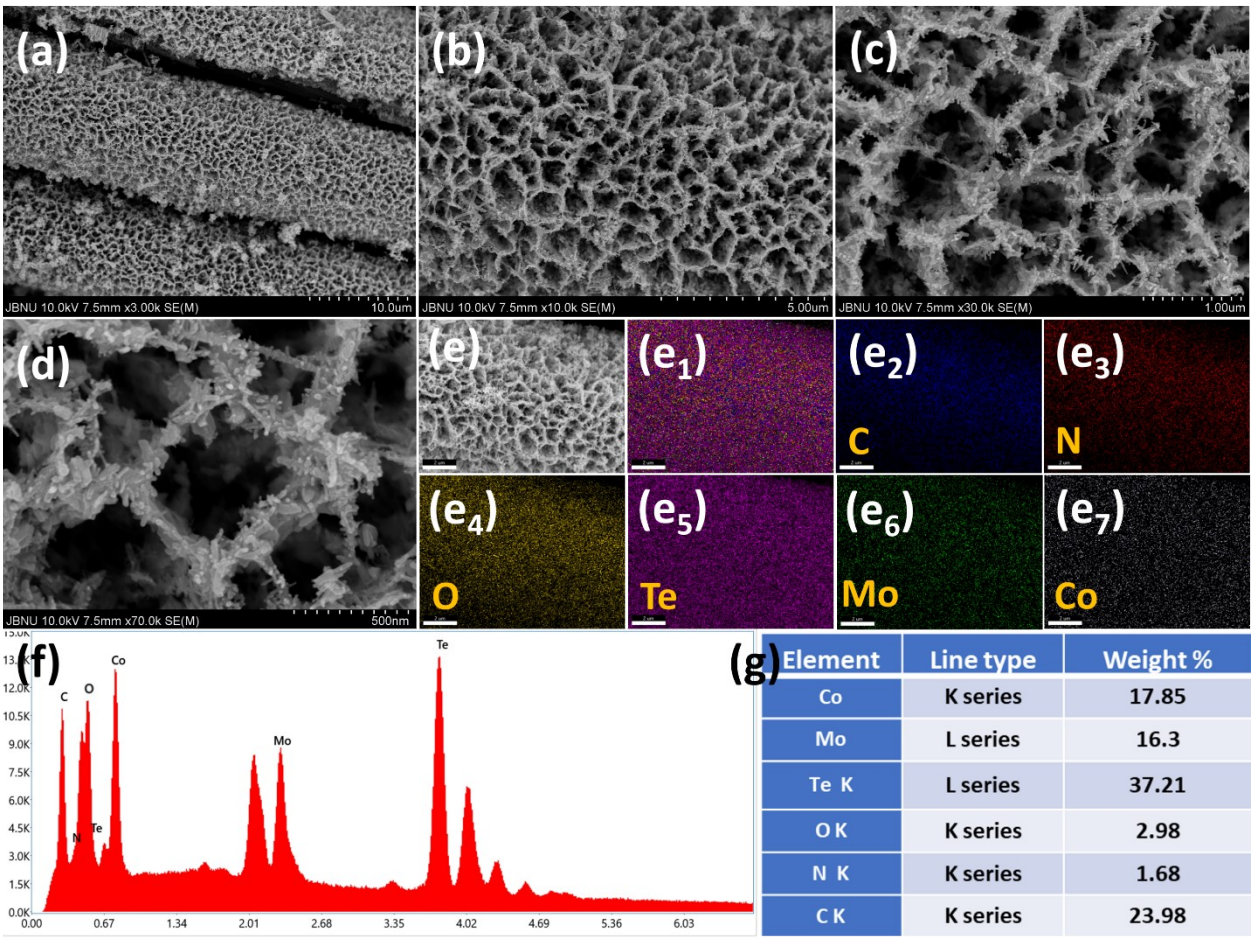

Element	Line type	Weight %
Co	K series	17.85
Mo	L series	16.3
Te K	L series	37.21
O K	K series	2.98
N K	K series	1.68
C K	K series	23.98

Fig. S5. (a-d) FESEM images of $CoTe_2/MoTe_2$@CC at different magnifications. EDX analysis of V-CoCHH@MX/HCF, (e) elemental mapping area, (e_1) superimposition of all elements, and elemental mapping spectra of (e_2) C, (e_3) N, (e_4) O, (e_5) Te, (e_6) Mo, and (e_7) Co, (f) corresponding EDX spectrum, and (j) weight % of different elements.

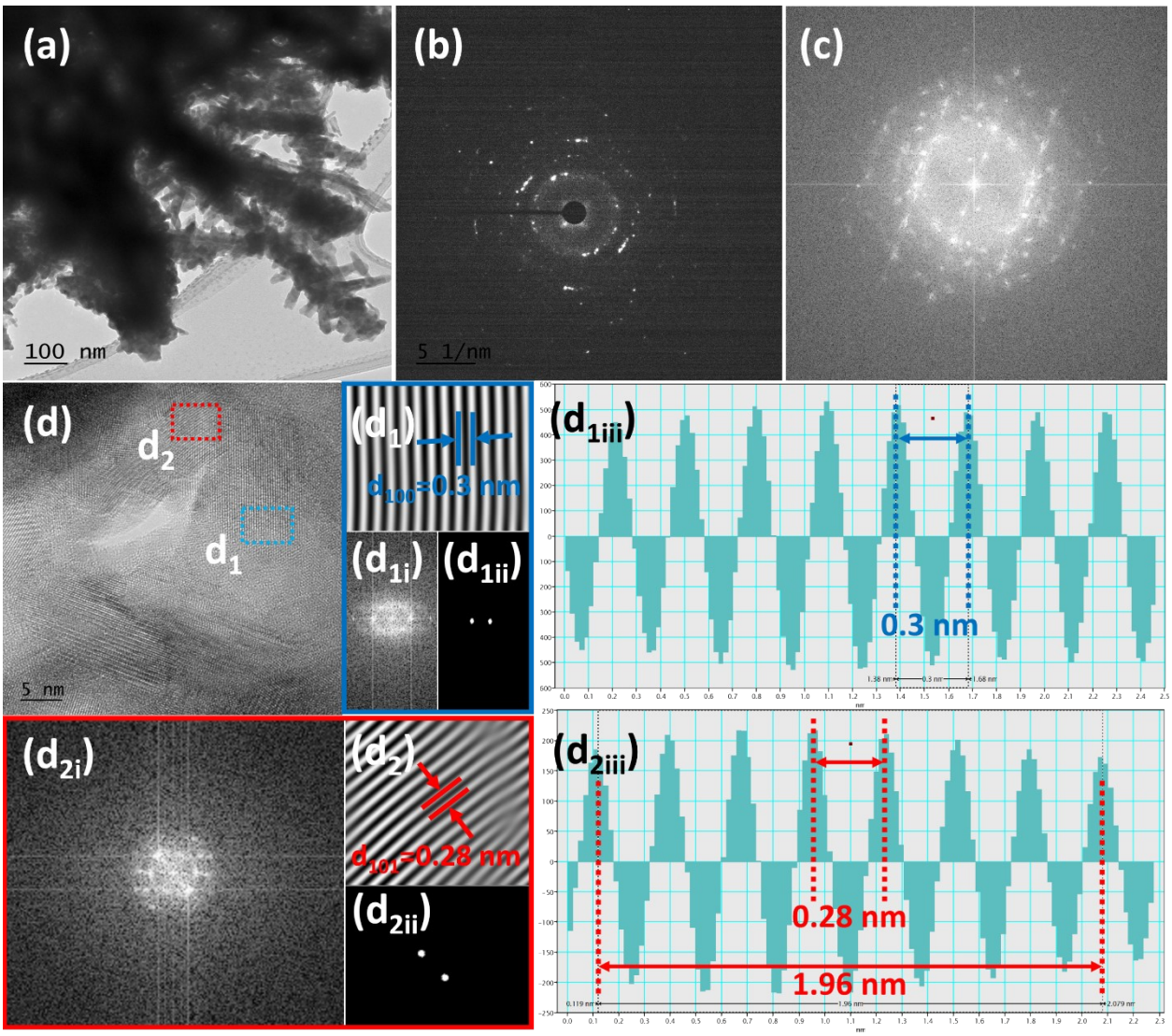

Fig. S6. TEM characterization of $CoTe_2/MoTe_2$@CC: (a) TEM image, (b) SAED patterns showing polycrystalline nature of the material, (c) corresponding FFT image, (d) HRTEM image, (d_1) lattice fringes of 0.3 nm corresponding to (100) plane of $MoTe_2$ derived from the selected region (blue dashed box) in (d), (d_{1i}) FFTs of selected region before applying the mask, (d_{1ii}) FFTs after applying the mask, (d_{1iii}) corresponding live profile graph, (d_2) lattice fringes of 0.28 nm corresponding to (101) plane of $CoTe_2$ derived from the selected region (red dashed box) in (d), (d_{2i}) FFTs of selected region before applying the mask, (d_{2ii}) FFTs after applying the mask, (d_{2iii}) corresponding live profile graph.

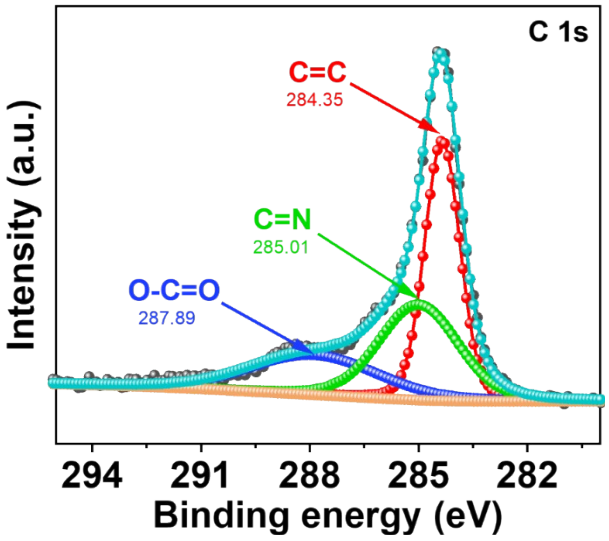

Fig. S7. High-resolution XPS spectra of V-CoTe2/MoTe2@CC deconvoluted for C 1s.

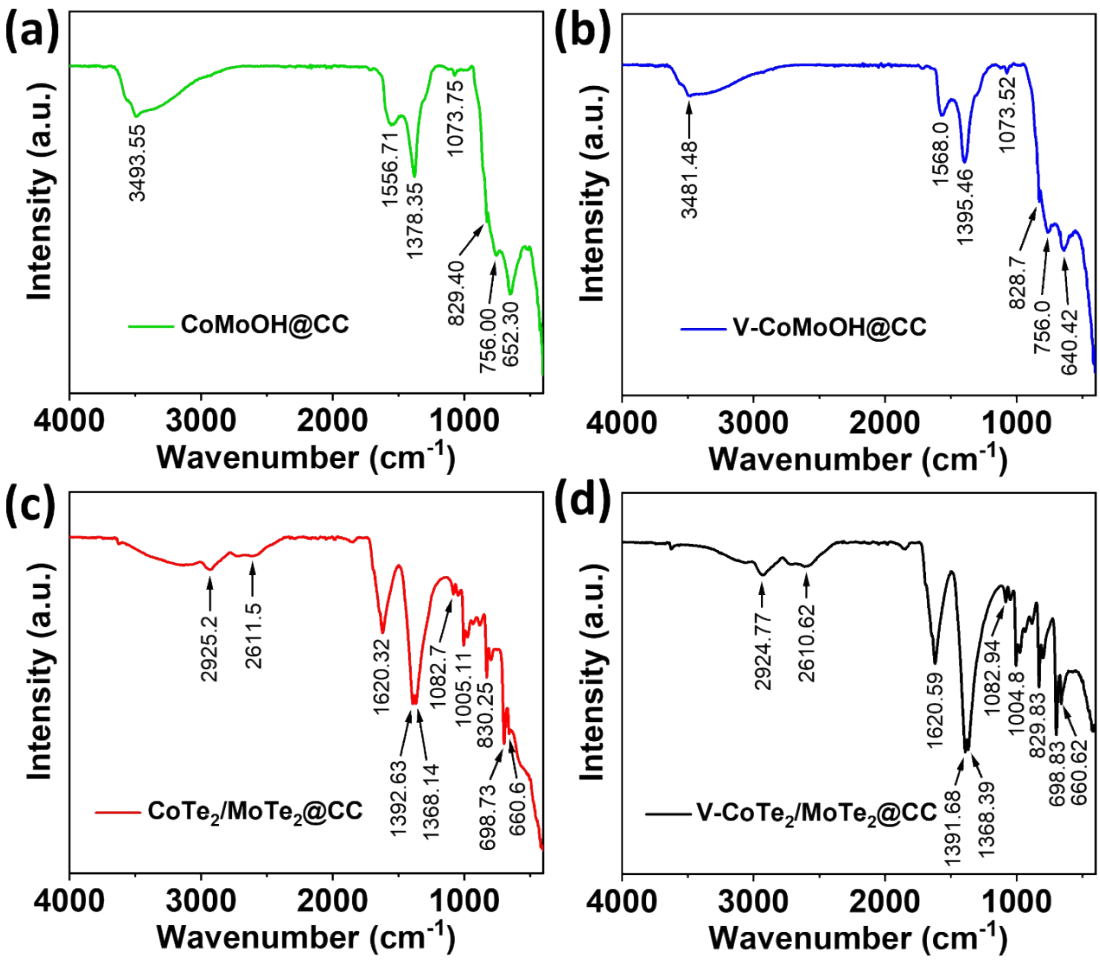

Fig. S8. FTIR spectra of (a) CoMoLDH@CC, (b)V-CoMoLDH@CC, (c) $CoTe_2/MoTe_2$@CC, and (d) V-$CoTe_2/MoTe_2$@CC.

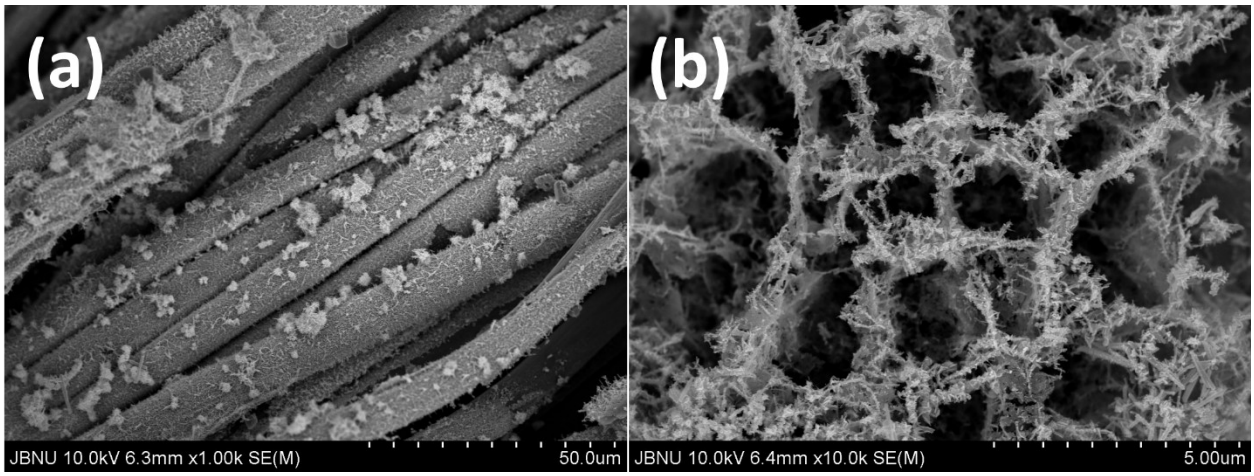

Fig. S9. (a,b) FESEM images of V-$CoTe_2$/$MoTe_2$@CC after HER test.

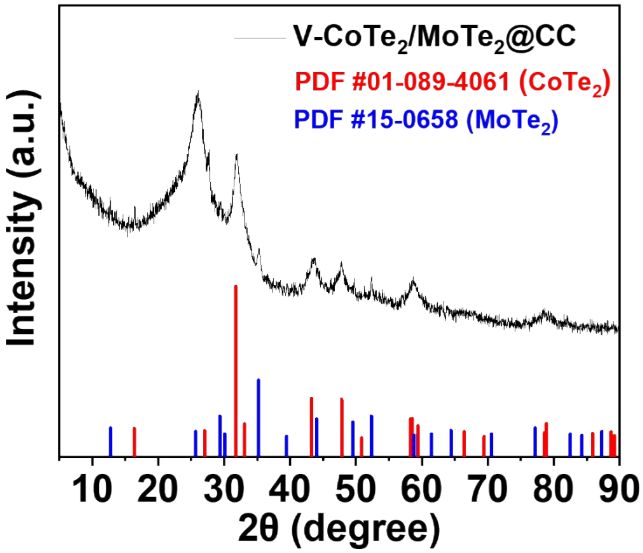

Fig. S10. XRD patterns of V-$CoTe_2$/$MoTe_2$@CC after HER test.

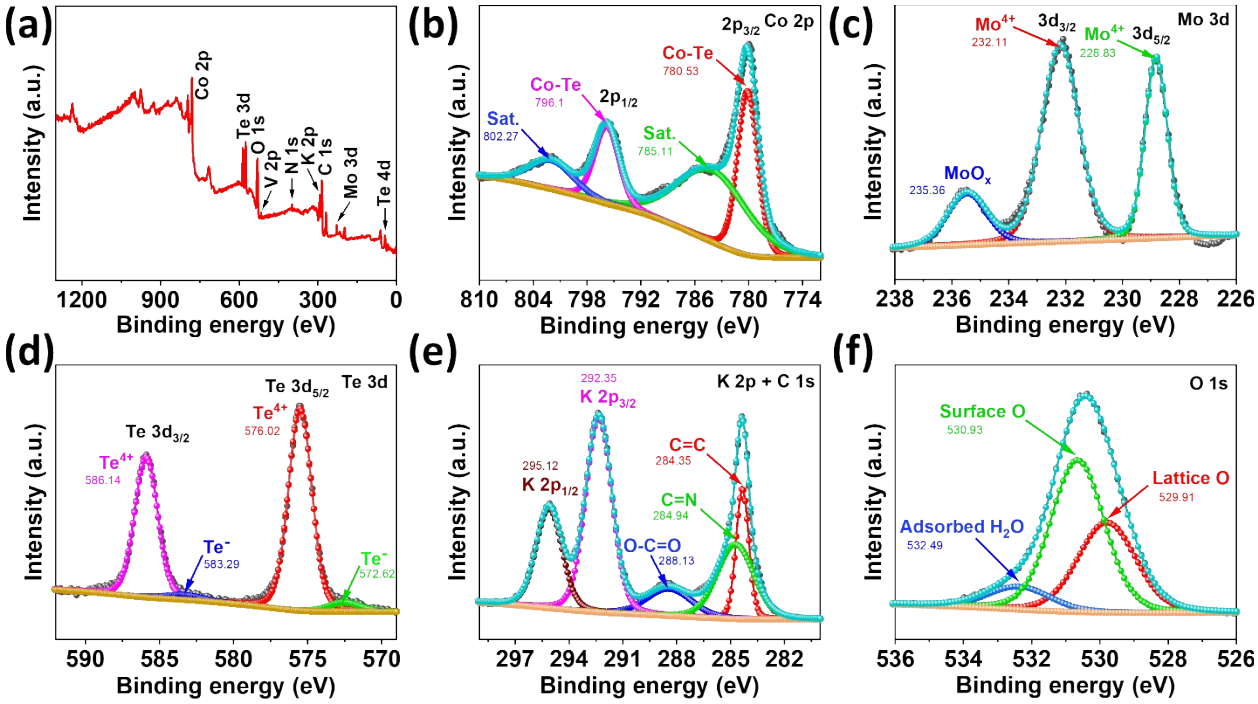

Fig. S11. XPS characterization of V-$CoTe_2$/$MoTe_2$@CC after HER test. (a) Low-resolution spectra, and high-resolution spectra of (b) Co 2p, (c) Mo 3d, (d) Te 3d, (e) K 2p + C 1s, and (f) O 1s.

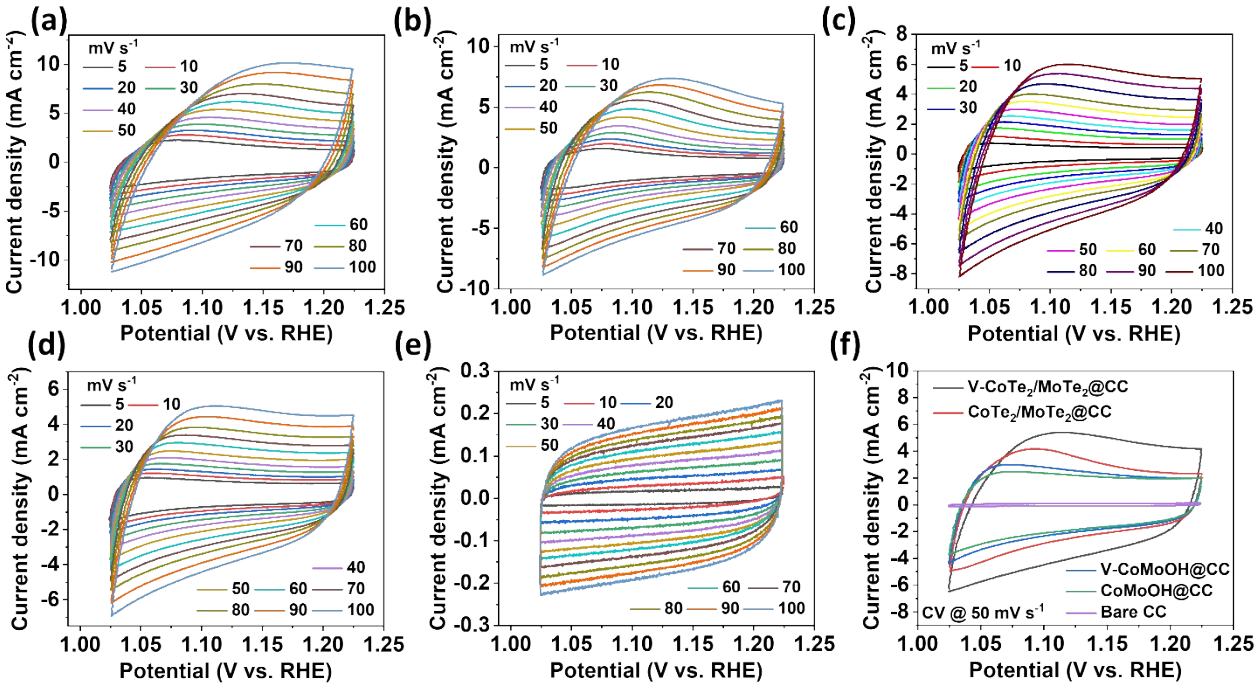

Fig. S12. C_{dl} calculation: CV curves of (a) V-$CoTe_2$/$MoTe_2$@CC, (b) $CoTe_2$/$MoTe_2$@CC, (c) V-CoMoOH@CC, (d) CoMoOH@CC, and (e) bare carbon cloth at scan rate from 5 to 100 mV s^{-1},

and (f) CV curves of different electrodes at 50 mV s^{-1} in 1 M KOH solution for OER.

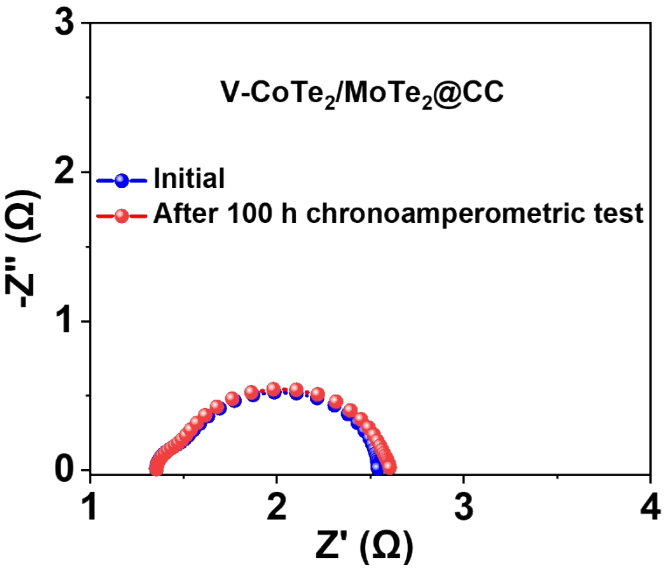

Fig. S13. Nyquist plot of V-$CoTe_2$/$MoTe_2$@CC before and after OER stability test.

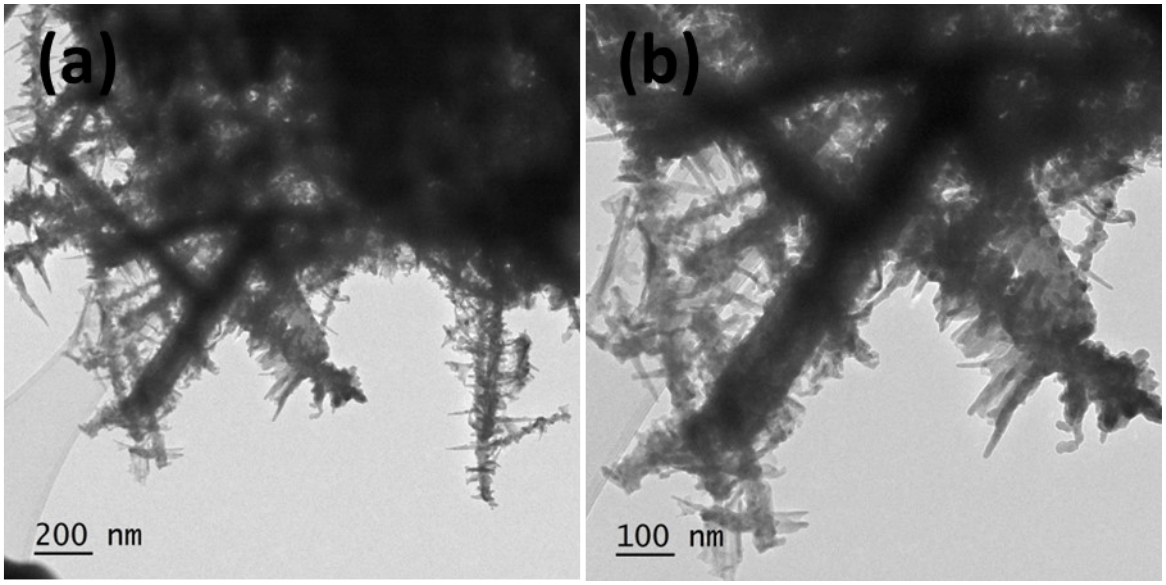

Fig. S14. (a,b) TEM images of V-$CoTe_2$/$MoTe_2$@CC after OER electrolysis in 1 M KOH for 100 h.

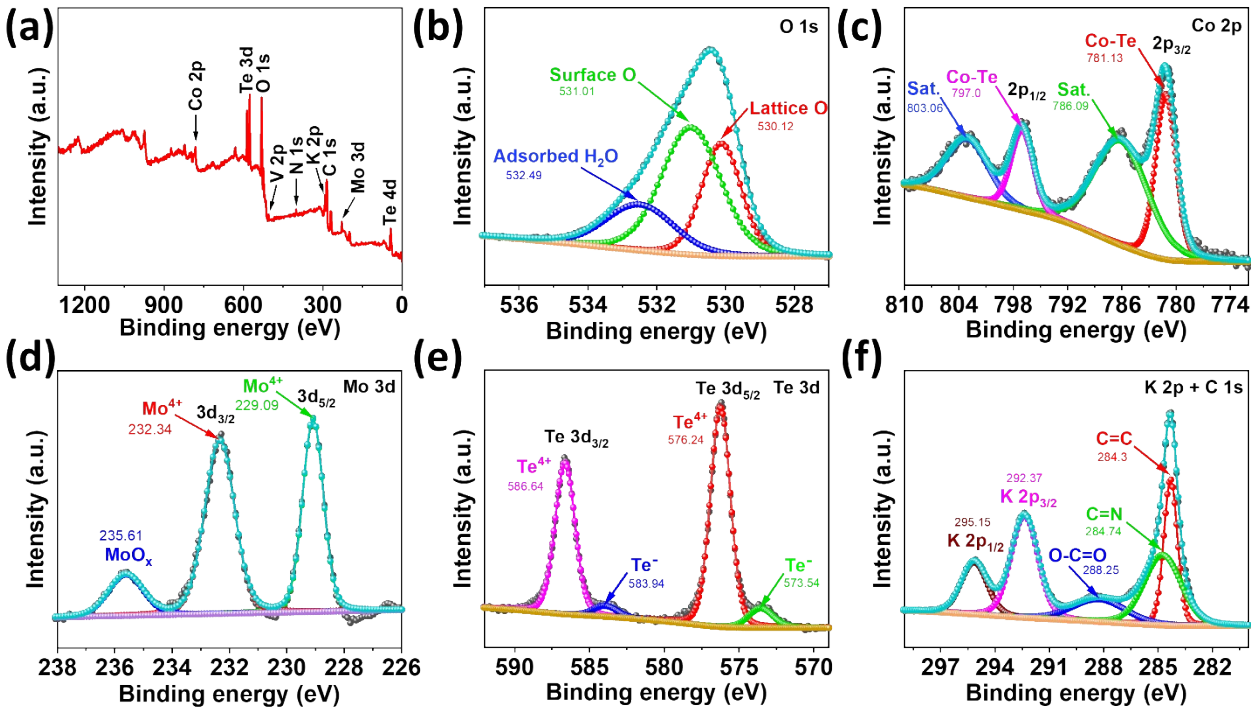

Fig. S15. XPS characterization of V-$CoTe_2$/$MoTe_2$@CC after OER test. (a) Low-resolution spectra, and high-resolution spectra of (b) O 1s, (c) Co 2p, (d) Mo 3d, (e) Te 3d, and (f) K 2p + C 1s.

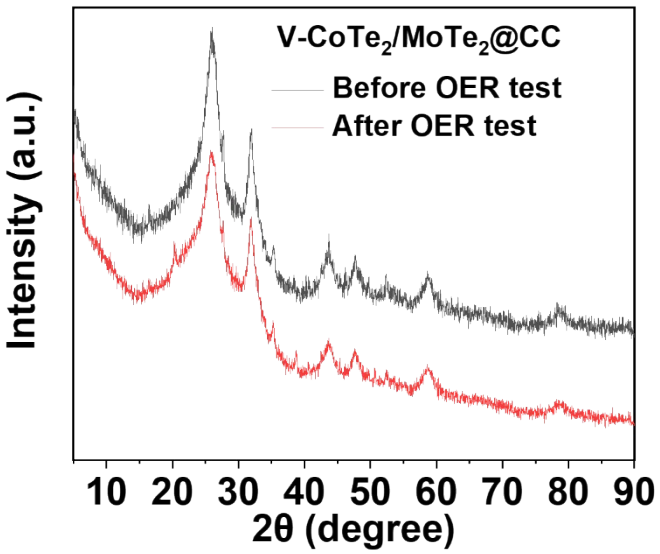

Fig. S16. XRD patterns of V-$CoTe_2$/$MoTe_2$@CC before and after OER test.

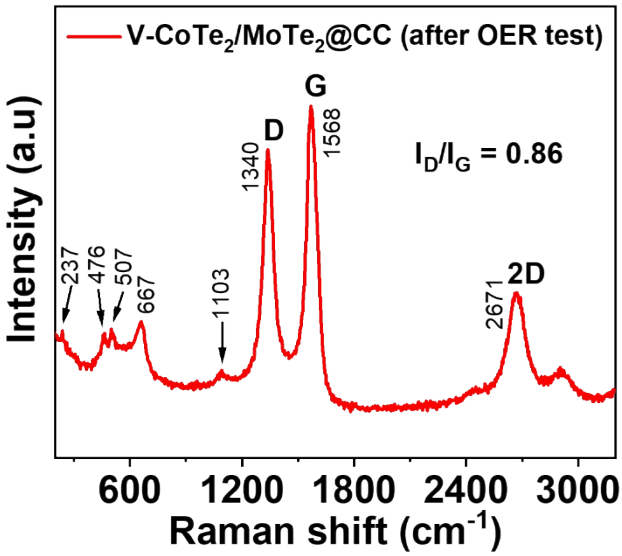

Fig. S17. Raman spectrum of V-$CoTe_2$/$MoTe_2$@CC after 100 h OER stability test.

Table S1: Atomic % of different elements observed in the XPS survey spectrum.

Element	**Atomic % of elements in**	
	V-$CoTe_2$/$MoTe_2$@CC	**$CoTe_2$/$MoTe_2$@CC**
Co 2p	14.32	15.96
Mo 3d	12.1	13.35
V 2p	4.06	0.00
Te 3d	38.89	36.81
O 1s	6.56	6.08
N 1s	2.41	2.3
C 1s	21.66	24.5

Table S2: Elemental compositions of V-$CoTe_2$/$MoTe_2$@CC determined with ICP-OES analysis.

Element	**Atomic %**
Co	23.89
Mo	21.25
V	7.47
Te	47.39

Table S3: The BET surface area, the total pore volume, and the average pore diameter of different samples.

Samples	V-$CoTe_2$/$MoTe_2$@CC	$CoTe_2$/$MoTe_2$@CC
BET surface area (m^2 g^{-1})	279.5	225.2
Total pore volume (cm^3 g^{-1})	0.481	0.324
Average pore diameter (nm)	5.5	5.1

Table S4. Comparison table for HER performance with recently reported similar electrocatalysts.

S.N.	Electrocatalysts	substrate	Electrolyte	Overpotential @ 10 mA cm^{-2} (mV)	Tafel slope (mV dec^{-1})	Ref.
1.	Co_6Mo_6C/MoC/Co	nickel foam	1 M KOH	52	54	[1]
2.	$Co_5Mo_{10}S_x$/CC	carbon cloth	1 M KOH	36	56	[2]
5.	Te-$CoMoO_3$@C	carbon matrix	1 M KOH	76	-	[3]
6.	$Co_{0.677}V_{0.33}P$@CC	carbon cloth	1 M KOH	77	-	[4]
7.	$CoTe_2$/CoP	Ti mesh	1 M KOH	80	57	[5]
8.	CoMoVLDH/NF	nickel foam	1 M KOH	150	182	[6]
9.	CC/MOF-$CoSe_2$@$MoSe_2$	carbon cloth	1 M KOH	109.87	68.91	[7]
10.	MoS_2@$Co_{1.11}Te_2$/Co-NCD-T	nickel foam	1 M KOH	124	49	[8]
11.	SeMoTe	nickel foam	1 M KOH	85	70	[9]
12.	$Co_{1.11}Te_2$/Te (Te-Co-3)	nickel foam	1 M KOH	135	56	[10]
13.	o-$CoSe_2$/c-$CoSe_2$/$MoSe_2$	carbon cloth	1 M KOH	112	96.9	[11]
14.	**V-$CoTe_2$/$MoTe_2$@CC**	**Carbon cloth**	**1 M KOH**	**79**	**58.9**	**This work**

Table S5. Comparison table for OER performance with recently reported similar electrocatalysts.

S.N.	Electrocatalysts	substrate	Electrolyte	Overpotential @ 10 mA cm^{-2} (mV)	Tafel slope (mV dec^{-1})	Ref.
1.	Co_6Mo_6C/MoC/Co	nickel foam	1 M KOH	223	106	[1]
2.	$Co_5Mo_{10}S_x$/CC	carbon cloth	1 M KOH	153	57.8	[2]
3.	Te-$CoMoO_3$@C	carbon matrix	1 M KOH	215	64	[3]
4.	$Co_{0.677}V_{0.33}$P@CC	carbon cloth	1 M KOH	290	55.59	[4]
5.	$CoTe_2$/CoP	Ti mesh	1 M KOH	260	89	[5]
6.	CoMoVLDH/NF	nickel foam	1 M KOH	270	106	[6]
7.	$Co_{1.11}Te_2$/Te	nickel foam	1 M KOH	261	52.6	[10]
8.	$Co_{0.50}Mo_{0.50}Te_2$	nickel foam	1 M KOH	160	62	[12]
9.	CoO@S-CoTe	nickel foam	1 M KOH	246	56	[13]
10.	S-CoTe/CC	carbon cloth	1 M KOH	257	63	[14]
11.	CoTe	glassy carbon	1 M KOH	316	86	[15]
12.	**V-$CoTe_2$/$MoTe_2$@CC**	**carbon cloth**	**1 M KOH**	**249**	**57.7**	**This work**

Table S6. Comparison table for overall full cell water-splitting performance with recently reported similar electrocatalysts.

S.N.	Electrocatalysts	substrate	Electrolyte	Cell Voltage @ 10 mA cm^{-2} (V)	Ref.
1.	Co-Mo-0.125-6N // Co-Mo-0.125-6N	nickel foam	1 M KOH	1.53	[1]

2.	$Co_5Mo_{10}S_x$/CC // $Co_5Mo_{10}S_x$/CC	carbon cloth	1 M KOH	1.51	[2]
4.	Te-$CoMoO_3$@C // Te-$CoMoO_3$@C	carbon matrix	1 M KOH	1.54	[3]
5.	$Co_{0.677}V_{0.33}P$@CC // $Co_{0.677}V_{0.33}P$@CC	carbon cloth	1 M KOH	1.61	[4]
7.	CoMoVLDH/NF // CoMoVLDH/NF	nickel foam	1 M KOH	1.61	[6]
8.	CC/MOF-$CoSe_2$@$MoSe_2$ // CC/MOF-$CoSe_2$@$MoSe_2$	carbon cloth	1 M KOH	1.53	[7]
6.	$Co_{1.11}Te_2$/Te (Te-Co-3) // $Co_{1.11}Te_2$/Te (Te-Co-3)	nickel foam	1 M KOH	1.56	[10]
9.	o-$CoSe_2$/c-$CoSe_2$/$MoSe_2$ // o-$CoSe_2$/c-$CoSe_2$/$MoSe_2$	carbon cloth	1 M KOH	1.63	[11]
3.	$Co_{0.50}Mo_{0.50}Te_2$ // $Co_{0.50}Mo_{0.50}Te_2$	nickel foam	1 M KOH	1.39	[12]
10.	**V-$CoTe_2$/$MoTe_2$@CC // V-$CoTe_2$/$MoTe_2$@CC**	**carbon cloth**	**1 M KOH**	**1.51**	**This work**

References:

1. X. Zhang, A. Wu, D. Wang, Y. Jiao, H. Yan, C. Jin, Y. Xie and C. Tian, *Applied Catalysis B: Environmental*, 2023, **328**, 122474.
2. Y. Lu, X. Guo, L. Yang, W. Yang, W. Sun, Y. Tuo, Y. Zhou, S. Wang, Y. Pan, W. Yan, D. Sun and Y. Liu, *Chemical Engineering Journal*, 2020, **394**, 124849.
3. L. Wang, H. Yu, S. Zhao, H. Ma, L. Li, F. Hu, L. Li, H. Pan, K. M. El-Khatib and S. Peng, *Inorganic Chemistry Frontiers*, 2022, **9**, 3788-3796.
4. H. Han, F. Yi, S. Choi, J. Kim, J. Kwon, K. Park and T. Song, *Journal of Alloys and Compounds*, 2020, **846**, 156350.
5. L. Yang, X. Cao, X. Wang, Q. Wang and L. Jiao, *Applied Catalysis B: Environmental*, 2023, **329**, 122551.
6. J. Bao, Z. Wang, J. Xie, L. Xu, F. Lei, M. Guan, Y. Zhao, Y. Huang and H. Li, *Chemical Communications*, 2019, **55**, 3521-3524.
7. S. J. Patil, N. R. Chodankar, S.-K. Hwang, P. A. Shinde, G. Seeta Rama Raju, K. Shanmugam Ranjith, Y. S. Huh and Y.-K. Han, *Chemical Engineering Journal*, 2022, **429**, 132379.
8. Z. Liu, S. Yun, M. Sun, J. Dang, Y. Zhang, Y. Wang, C. Dang, Y. Deng and D. Qiao, *Materials Today Nano*, 2022, **20**, 100274.
9. D. Vikraman, S. Hussain, I. Rabani, A. Feroze, M. Ali, Y.-S. Seo, S.-H. Chun, J. Jung and H.-S. Kim, *Nano Energy*, 2021, **87**, 106161.

10. G. Wang, C. Hua, W. Chen, H. Fan, P. Feng and Y. Zhu, *Electrochimica Acta*, 2023, **447**, 142133.
11. Y. Ji, W. Luo, Y. Liu, Z. He, N. Cheng, Z. Zhang, X. Qi, J. Zhong and L. Ren, *Materials Today Chemistry*, 2022, **23**, 100724.
12. D. Vikraman, S. Hussain, Z. Abbas, K. Karuppasamy, P. Santhoshkumar, J. Jung and H.-S. Kim, *ACS Applied Materials & Interfaces*, 2023, **15**, 26893-26909.
13. X. Wang, Z. Mao, X. Mao, X. Hu, F. Gao, M. Gao, Q.-L. Wu, X. Lyu, A. Du, X. Xu, Y. Jia and L. Wang, *Advanced Science*, 2023, **10**, 2206204.
14. L. Yang, H. Qin, Z. Dong, T. Wang, G. Wang and L. Jiao, *Small*, 2021, **17**, 2102027.
15. D. A. Alshammari, Y. M. Riyad, S. Aman, N. Ahmad, H. M. Tahir Farid and Z. M. El-Bahy, *Journal of Electroanalytical Chemistry*, 2023, **945**, 117701.